nanomaterials

MDPI

Article

Hydrothermal Synthesis of Nanooctahedra $MnFe_2O_4$ onto the Wood Surface with Soft Magnetism, Fire Resistance and Electromagnetic Wave Absorption

Hanwei Wang [1], Qiufang Yao [1], Chao Wang [1], Zhongqing Ma [1], Qingfeng Sun [1,2,*], Bitao Fan [1], Chunde Jin [1,2] and Yipeng Chen [1]

[1] School of Engineering, Zhejiang Agriculture & Forestry University, Lin'an 311300, China; 18868196590@163.com (H.W.); yaoqiufang105@163.com (Q.Y.); chaowangzafu@163.com (C.W.); mazqzafu@163.com (Z.M.); 18357178962@163.com (B.F.); jincd@zafu.edu.cn (C.J.); 18868195633@sina.cn (Y.C.)

[2] Key Laboratory of Wood Science and Technology, Hangzhou 311300, China

* Correspondence: qfsun@zafu.edu.cn; Tel./Fax: +86-571-6373-2718

Academic Editor: Jordi Sort

Received: 9 February 2017; Accepted: 8 May 2017; Published: 23 May 2017

Abstract: In this study, nanooctahedra $MnFe_2O_4$ were successfully deposited on a wood surface via a low hydrothermal treatment by hydrogen bonding interactions. As-prepared $MnFe_2O_4$/wood composite (MW) had superior performance of soft magnetism, fire resistance and electromagnetic wave absorption. Among them, small hysteresis loops and low coercivity (<±5 Oe) were observed in the magnetization-field curve of MW with saturation magnetization of 28.24 emu/g, indicating its excellent soft magnetism. The MW also exhibited a good fire-resistant property due to its initial burning time at 20 s; while only 6 s for the untreated wood (UW) in combustion experiments. Additionally, this composite revealed good electromagnetic wave absorption with a minimum reflection loss of −9.3 dB at 16.48 GHz. Therefore, the MW has great potential in the fields of special decoration and indoor electromagnetic wave absorbers.

Keywords: wood; $MnFe_2O_4$/wood composite; hydrothermal; soft magnetism; fire resistance; electromagnetic wave absorption

1. Introduction

Wood/inorganic hybrids fall under the category of new functional nanocomposite materials because of being a combination between organic and inorganic materials with their respective advantages and excellent performance. Synergistic effects resulting from the physical or chemical interactions between the inorganic and wood components have produced such properties as improved thermal stability, UV-resistance, hydrophobic, mechanical and dimensional stability [1]. Currently, deposition of a thin solid inorganic nanomaterial coating imbedded onto the wood surface has great potential to improve the inherent wood defects (like moisture deformation, easily burnt, etc.) and simultaneously to grant novel performances (like super-hydrophobic, self-cleaning, UV–resistance, or others) [2]. The present focus among the thin solid inorganic nanomaterial coatings is mainly metal semiconductor materials, like TiO_2 [3,4], SiO_2 [5], ZnO [6], CeO_2 [7], and so on [8–13]. Several research works paid less attention to magnetic nanostructure materials deposited onto the wood surface.

With the rapid development of wireless communications indoors and outdoors, the electromagnetic interference (EMI) pollution has become much more serious. The electromagnetic waves may cause interception and malfunction of the performance of electrical equipment in medical, military and aircraft systems or even lead to radiative damage of the human body [7,14]. Therefore, it

is necessary to exploit new types of microwave-absorption materials with excellent properties, such as a wide frequency range, strong absorption, low density, high resistivity, etc.

Magnetic nanomaterials/wood hybrids would be potential candidates for microwave absorption, especially when wood serves as interior decorations due to its renewability, attractive surface, sound insulation, temperature- and humidity-controlling performances. It may be a reasonable choice for wave absorption if the wood surface is embedded with a thin solid magnetic film with a trivial change of appearance. Previous studies have been conducted showing that the wood surface can be considered as an effective substrate containing plentiful hydroxyl groups for the nucleation and growth of inorganic nanomaterials. Publicly reported pathways for the deposition of magnetic materials are the sol-gel method [15–17], electroless deposition [18], the hydrothermal process [19,20] and physical padding. Among these methods, the hydrothermal method was a feasible and efficient pathway for growing magnetic nanomaterials with high product purity and homogeneity, crystal symmetry, narrow particle size distributions, a lower sintering temperature, a wide range of chemical compositions and single-step processes, as well as for the growth of crystals with polymorphic modifications [21–27]. Herein, we employed a facile low temperature hydrothermal process for the growth of nanooctahedra $MnFe_2O_4$ on the wood surface. The as-prepared $MnFe_2O_4$/wood (MW) composite showed a superior soft magnetism, fire resistance and electromagnetic absorption. The saturation magnetization of the MW was 28.24 emu/g with extremely small hysteresis loops, and low coercivity indicated that this composite was an excellent soft-magnetic material. The MW also exhibited a good fire resistance property due to it not being burnt in the first 20 s, while only 6 s were needed for the untreated wood. Additionally, this composite is a good electromagnetic absorption material due to its minimum reflection loss of −9.3 dB at 16.48 GHz. Thus, the MW has great potential in the fields of special decoration and indoor electromagnetic wave absorbers.

2. Experimental Details

2.1. Materials

All chemicals were supplied by Boyle chemical Co. Ltd., Shanghai, China. and used without further purification. The wood slices were cut with sizes of 20 mm (length) × 10 mm (width) × 5 mm (height), and then, the slices were ultrasonically rinsed in deionized water for 30 min and dried at 80 °C in a vacuum.

2.2. One-Pot Hydrothermal Synthesis of MW

In a typical synthesis, $FeCl_3 \cdot 6H_2O$ and $MnSO_4 \cdot H_2O$ in a stoichiometric ratio of 2:1 were dissolved in 80 mL of deionized water under magnetic stirring at room temperature. The obtained homogeneous mixture was transferred into a 100 mL Teflon-lined stainless autoclave. Wood specimens were subsequently placed into the above reaction solution, and the pH value was adjusted via adding a certain amount of ammonia solution. The Teflon-lined stainless-steel autoclave was sealed and heated to 120 °C for 8 h. Subsequently, the autoclave was left to cool down to room temperature. Finally, the prepared magnetic wood samples were removed from the solution, ultrasonically rinsed with deionized water for 30 min and dried at 45 °C for over 24 h in a vacuum.

2.3. Characterizations

The surface morphologies of the samples were characterized by scanning electron microscopy (SEM, Quanta 200, FEI, Eindhoven, The Netherlands). Crystalline structures of the samples were identified by the X-ray diffraction technique (XRD, D/MAX 2200, Rigaku, Tokyo, Japan) operating with Cu Kα radiation (λ = 1.5418 Å) at a scan rate (2θ) of 4° min^{-1}, an accelerating voltage of 40 kV and the applied current of 30 mA ranging from 10–80°. Changes of chemical groups were recorded via a Fourier transform infrared spectroscopy (FT-IR, Magna-IR 560, Nicolet, Madison, WI, USA). XPS analysis was characterized by an X-ray photoelectron spectrometer (XPS, ESCALAB 250 XI, Thermofisher Co.,

Bridgewater, NJ, USA). The magnetic properties of the composites were measured by a vibrating sample magnetometer (VSM, Model 7404, LakeShore Cryotronics Inc., Westerville, OH, USA) at 300 K. The thermal performances of the MW were examined using a thermal gravimetric analysis (TGA, SDT Q600, TA Instruments, New Castle, DE, USA) heating rate of 4 °C/min and under an N_2 flow rate of 50 mL/min. The relative permeability and permittivity were obtained on an Agilent N5244A PNA-X network analyzer (VNA, Agilent Technologies Inc., Richardson, TX, USA) in the frequency range of 2–18 GHz for the calculation of reflection loss (RL) by the coaxial reflection/transmission method based on the NRW (Nicolson-Ross-Weir) method. The sample containing composite materials and paraffin wax with the mass ratio of 2:3 was pressed into toroidal-shaped samples (Φout = 7.00 mm, Φin = 3.04 mm, thickness = 2 mm) for microwave measurement. The simulated reflection loss (RL) was calculated from the measured parameters according to the transmission line theory.

3. Results and Discussion

Figure 1a shows the XRD patterns of the untreated wood and the $MnFe_2O_4$/wood composite. The strong diffraction peaks at 16.1° and 22.6° were equivalent to the crystalline region of the cellulose of the wood (Figure 1a). In addition, the diffraction peaks at 17.9°, 30.3°, 35.6°, 43.3°, 53.5°, 57.1° and 62.8° could be attributed to the diffractions of the (111), (220), (311), (400), (422), (511) and (440), which confirmed the presence of the $MnFe_2O_4$ (JCPDS 73-1964) with a phase-pure spinel structure on the wood surface. This result revealed that the $MnFe_2O_4$ was successfully grown on the wood surface.

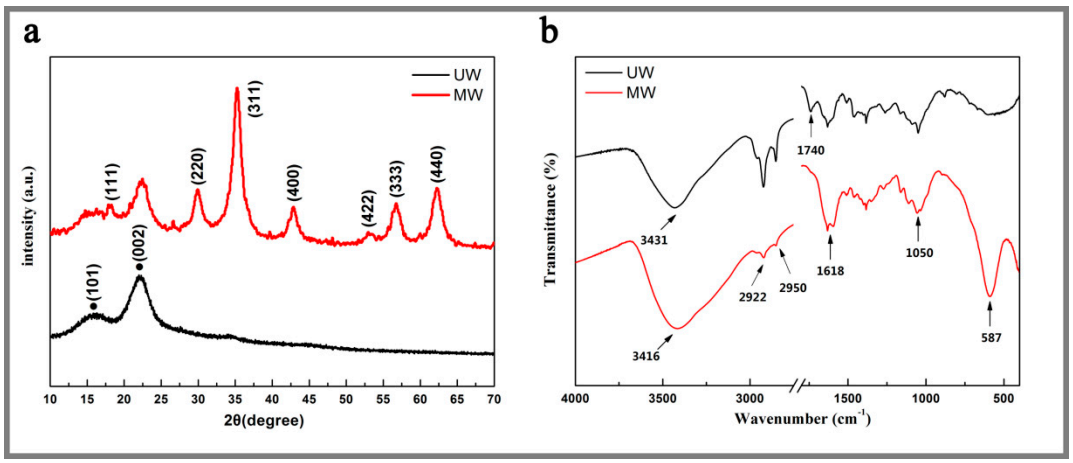

Figure 1. (**a**) XRD patterns and (**b**) FTIR spectra of the untreated wood (UW) and the $MnFe_2O_4$/wood composite (MW).

Figure 1b showed the FTIR spectra (400–4000 cm^{-1}) of the untreated wood (UW) and the MW. The main absorption bands of the MW were located at 3416 cm^{-1}, 1168 cm^{-1} and 1050 cm^{-1}, corresponding to the stretching vibrations of O–H, C=O and C–O, respectively, which were attributed to the chemical contents of the wood substrate (hemicellulose, cellulose and lignin). The peak of UW at 3431 cm^{-1} was ascribed to stretching vibrations of the hydroxyl groups of the wood. Then, this peak shifted to the lower wavenumbers of 3416 cm^{-1} after coating $MnFe_2O_4$ on the wood surface, indicating the formation of the hydrogen bonding interaction between the nanooctahedra $MnFe_2O_4$ and the wood [28]. The peaks at 2922 cm^{-1} and 2950 cm^{-1} were caused by the stretching vibrations of $–CH_3$ and $–CH_2$, but these peaks in the MW spectra significantly decreased; and the peak at 1740 cm^{-1} (the carbon and oxygen double bonds) only existed in the UW spectra [29]. These phenomena were attributed to the hydrolysis of fatty acids by hydrothermal reaction under the alkaline conditions. Simultaneously, the absorption peaks at 587 cm^{-1} were intrinsic vibrations of the manganese ferrite [29].

The surface morphologies of the UW and MW by scanning electron microscopy are exhibited in Figure 2. Some fibrils and the inner surface of the lumen could be clearly observed on the microstructure

of a longitudinal section of the UW surface. After the hydrothermal process, the wood surface was compactly covered by $MnFe_2O_4$ in Figure 2b. The inset of (b) shows the size distribution of nanooctahedra $MnFe_2O_4$ with an average particle size of 0.68 nm and a size distribution width of 0.5–1 µm. Figure 2c shows the $MnFe_2O_4$ with an octahedral shape aggregated over the wood surface by a compact manner, and many small nanoparticles also were equipped on this nanooctahedra $MnFe_2O_4$ surface. In order to further investigate the fine features of the nanooctahedra $MnFe_2O_4$, the MW was studied by a zoomed-in SEM after ultrasonic treatment with 1800 W for 30 min (Figure 2d). The zoomed-in SEM showed the nanooctahedra $MnFe_2O_4$ still tightly covered the wood surface, but a small fraction of the $MnFe_2O_4$ and the bare wood surface appeared to rupture. These results indicated that the nanooctahedra $MnFe_2O_4$ were closely integrated with the wood surface by a strong interaction. In addition, the surface of nanooctahedra $MnFe_2O_4$ became very clean, which might reveal that small nanoparticles were adsorbed on the surface of nanooctahedra $MnFe_2O_4$ by a physical process.

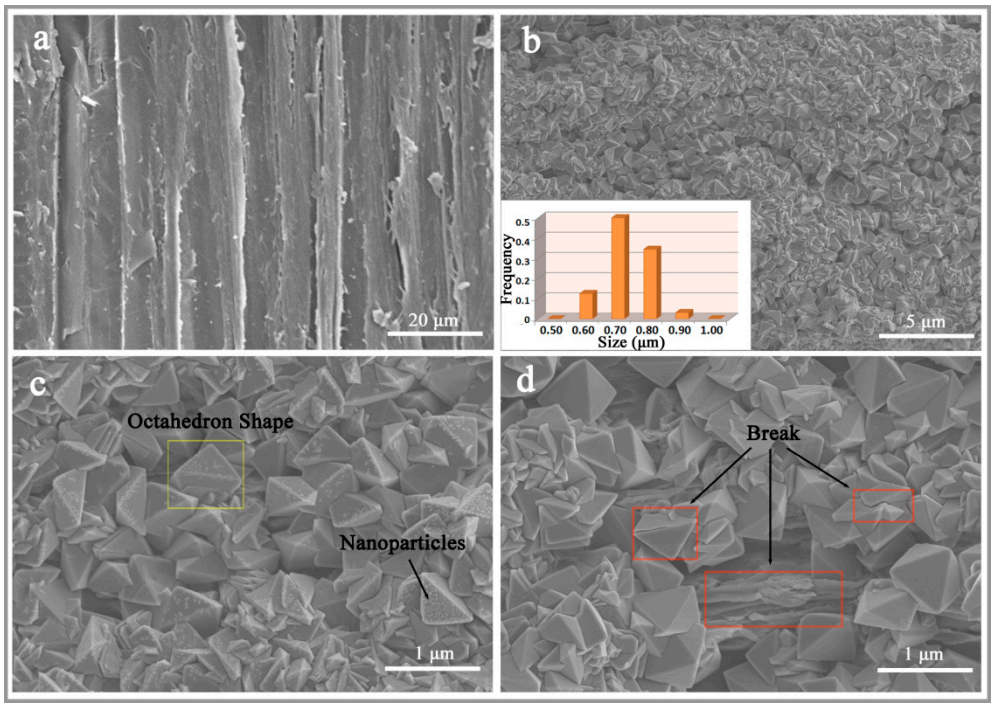

Figure 2. SEM images of (**a**) the surfaces of the UW; (**b**) the surfaces of the MW with low-magnification; (**c**) the surfaces of the MW without ultrasonic treatment and (**d**) the surfaces of the MW after ultrasonic treatment. The inset of (**b**) is the size distribution of nanooctahedra $MnFe_2O_4$.

X-ray photoelectron spectroscopy (XPS) is a powerful technique for studying the elemental composition and chemical oxidation state of the surfaces. Figure 3a shows the survey-scan XPS spectra of UW and MW; elemental O and C coexisted in both samples, where the C element was attributed to the wood substrate from cellulose, lignin and hemicellulose. In addition, besides O and C elements, the survey-scan spectrum of the MW revealed iron and manganese peaks, which should come from $MnFe_2O_4$ nanoparticles on the wood surface. Figure 3b,c shows the Fe2p and the Mn2p spectra, respectively. For Fe, the two main peaks $Fe2p_{1/2}$ and $Fe2p_{3/2}$ at 724.73 eV and 711.13 eV, respectively, indicate the presence of Fe^{3+} cations by comparison with the $Fe2p_{3/2}$ peaks of Fe_2O_3 and Fe metal [30–33]. Two sharp peaks for the $Mn2p_{1/2}$ and $Mn2p_{3/2}$ at 653.23 eV and 641.43 eV, respectively, indicate the presence of Mn^{2+} cations by comparison with the MnO [34].

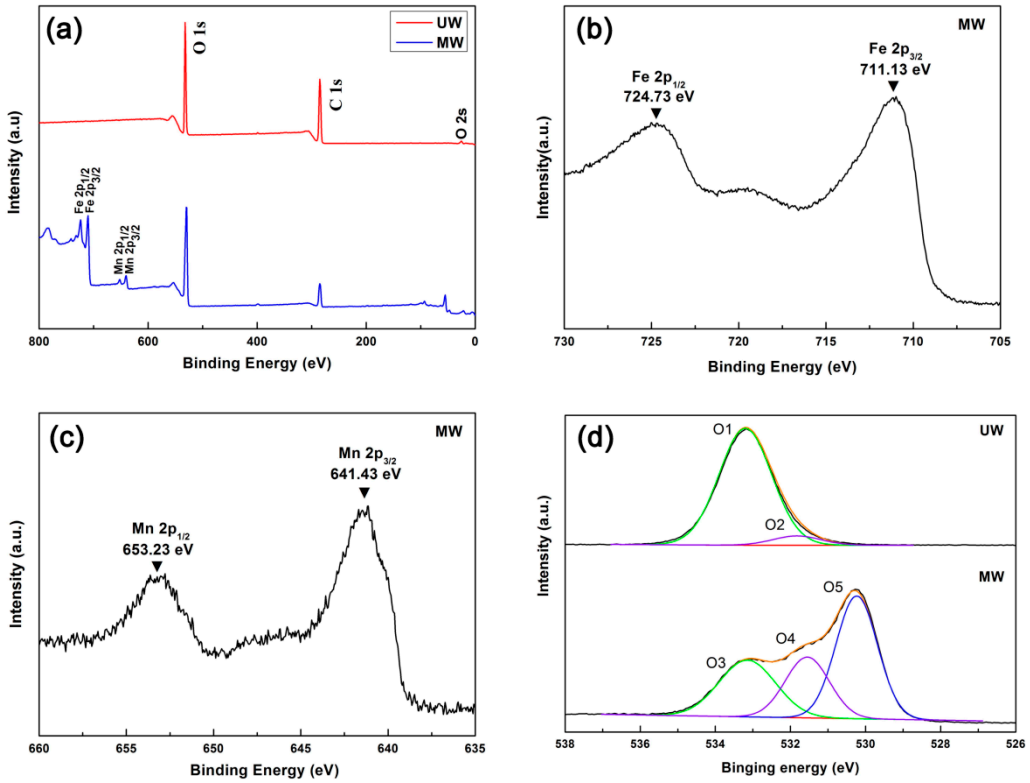

Figure 3. (**a**) Survey-scan XPS spectra of the UW and the MW; (**b**) Fe2p XPS spectra of the MW; (**c**) Mn2P XPS spectra of the MW; (**d**) O1s XPS spectra of the UW and MW.

Figure 3d and Table 1 illustrated the O1s spectra and binding energy of the UW and MW samples, respectively. The broad peak of O1s at the UW spectrum could be fitted by two peaks at binding energies of 533.18 eV and 531.83 eV, respectively. The largest peak at 533.18 eV was attributed to the carbon-oxygen bond on the wood, such as cellulose, lignin and hemicellulose. The other peak at 531.83 eV was assigned to the other oxygen from OH, H_2O and carbon-oxygen double bonds from the wood substrate. By contrasts, the main peak on the O1s spectrum of MW appeared at binding energies of 530.23 eV, which was compatible with oxygen in metal oxides, such as Fe–O and Mn–O [35,36]. Furthermore, it is easily observed that the peak at 531.82 eV had been shifted to 531.55 eV and relatively higher than before the reaction. That strongly indicated that the $MnFe_2O_4$ nanoparticles had been successfully located on the wood surface by the hydrogen bond after hydrothermal treatment under this work.

Table 1. Surface composition of the UW and the MW.

UW		MW		Assignment
The excited electron O1s	Binding energy (eV)	The excited electron O1s	Binding energy (eV)	
O1	533.18	O3	533.15	C–O
O2	531.83	O4	531.55	O–H, C=O
		O5	530.23	Mn–O, Fe–O

A mechanism of the formation of the nanooctahedra $MnFe_2O_4$ might be expressed by reaction Equations (1)–(3):

$$Fe^{3+} + 3OH^- \rightleftharpoons Fe(OH)_3(s); Mn^{2+} + 2OH^- \rightleftharpoons Mn(OH)_2(s) \quad (1)$$

$$Fe(OH)_3(s) + (n\text{-}3)OH^- \rightleftharpoons Fe(OH)_n^{3-n};\ Mn(OH)_2(s) + (n\text{-}2)OH^- \rightleftharpoons Mn(OH)_n^{2-n} \quad (2)$$

$$Mn(OH)_n^{2-n} + Fe(OH)_n^{3-n} \rightarrow MnFe_2O_4 + H_2O \quad (3)$$

On the basis of the results mentioned above, a schematic illustration of the creation of nanooctahedra $MnFe_2O_4$ on the wood surface through a low temperature hydrothermal process is proposed in Figure 4. The precursors ($FeCl_3 \cdot 6H_2O$ and $MnSO_4 \cdot H_2O$) were dissolved into the deionized water and provided Mn^{2+} and Fe^{3+} ions at first. After adding ammonia solution, the Mn^{2+} and Fe^{3+} ions with the hydroxyl ions in the solution transformed into Mn hydroxides and Fe hydroxides, respectively. The Fe and Mn hydroxides dissolved in the mixed solution because of the presence of high concentrations of the ammonia and converted to the $Mn(OH)_n^{2-n}$ and $Fe(OH)_n^{3-n}$ with massive hydroxyl groups. Then, the $Mn(OH)_n^{2-n}$ and $Fe(OH)_n^{3-n}$, as the growth unit, formed the $MnFe_2O_4$ nanocrystal nucleus by the dehydration reaction. Additionally, the plentiful hydroxyl groups of the wood surface absorbed the $MnFe_2O_4$ nanocrystal for its the OH-rich surface that could be due to the high surface activity and large surface-to-volume atomic ratio on the $MnFe_2O_4$ nanoparticle's surface. Finally, with the hydrothermal advanced, the $MnFe_2O_4$ nanocrystal developed a more stable $MnFe_2O_4$ layer on the wood surface and formed the $MnFe_2O_4$/wood composite.

Figure 4. Possible schematic illustration of the preparation of the MW.

Figure 5 shows the magnetization-field curves of MW at 298 K. The saturation magnetization of MW was 28.24 emu/g, and it exhibited small hysteresis loops and low coercivity (<±5 Oe), as shown in the inset (a). Therefore, the MW showed a soft magnetism behavior [37–39]. The lower right corner illustration shows the camera images of the magnet attracting samples. In the inset (b), the UW lacks the response by a magnet, and the MW could be easily removed from the desktop by a magnet. These results revealed that the MW is an excellent soft magnetic material with sensitive magnetic response [40].

The thermal stability of MW and UW was determined by TG and DTG under nitrogen atmosphere as shown in Figure 6. In the first stage (20 °C–110 °C), a little weight loss (UW of 7.43%; MW of 4.52%) was observed, which was related to the release of moisture from the samples. Thus, the water content of the UW and MW was 7.43% and 4.52%, respectively. In the second stage (110–410 °C), the weight/mass-loss rates of UW and MW were approximately 68.37% and 16.80%, respectively. The main weight loss was mainly attributed to the pyrogenic decomposition of hemicellulose and cellulose. The pyrolysis maximum rates of UW and MW occurred at 364 and 380 °C, respectively. Furthermore, the maximum rate of UW of −0.2189%/°C was higher than MW −1.049%/°C on the DTG curves, which could be caused by the higher content of nanooctahedra $MnFe_2O_4$ on the samples. In the third stage (410–800 °C), the weight loss of the MW reaches, 10.15% and the maximum pyrolysis rate occurred at 570 °C in which the nanooctahedra $MnFe_2O_4$ protects and improves the pyrolysis temperature of the wood. Finally, the MW still had larger residues (68.53%) with carbon residues and $MnFe_2O_4$, while the remainder of the UW with carbon residues was only 14.31% at 800 °C. This

phenomenon indicated that the nanooctahedra $MnFe_2O_4$ deposited on the wood surface and had a large proportion in the MW. In summary, the thermal stability of the wood had been improved after the hydrothermal reaction and the existence of the potential in the fire-resistant performance.

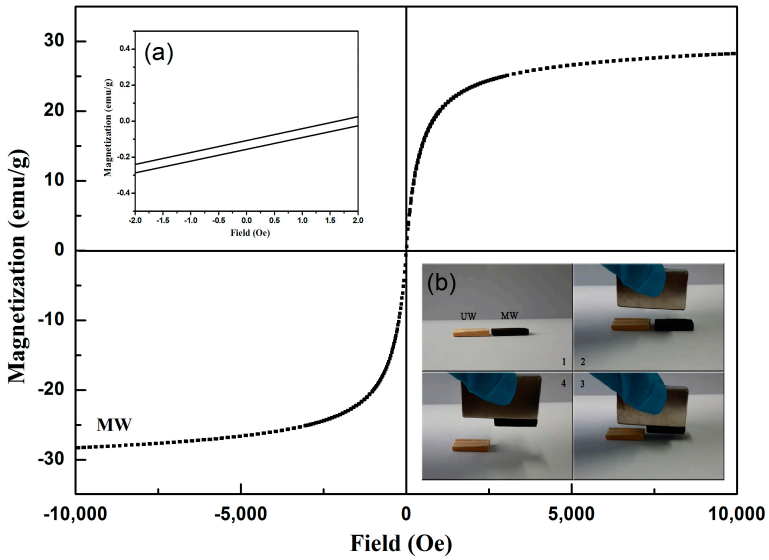

Figure 5. Magnetization of the MW as a function of the applied magnetic field. The inset (**a**) shows a magnification of one segment of the MW magnetization-field curves, and the inset (**b**) shows that the UW and MW samples were attracted by a magnet.

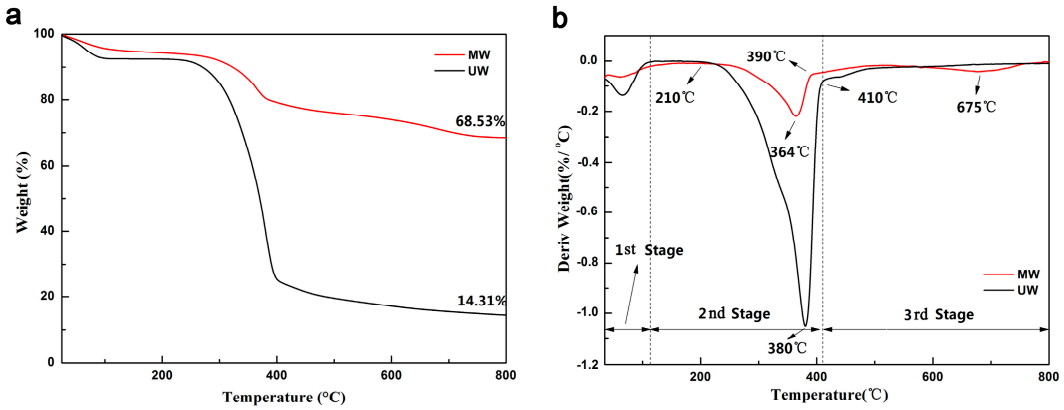

Figure 6. (**a**) Thermogravimetric (TG) and (**b**) differential thermogravimetric (DTG) curves of the UW and the MW under a nitrogen atmosphere.

In order to test the fire-resistant property, it was of great significance to test the ignitability of the UW and MW on an alcohol lamp flame. Figure 7 shows the digital photos of the UW and the MW on the alcohol lamp flame for the first 20 s. In Figure 7a, the UW caught on fire at 6 s and was incinerated to ash after 70 s. After removing the alcohol lamp at 20 s, the flames still burned strongly until 35 s. After 35 s, the flame had been gradually extinguished, and it became ash. By contrast, the MW could not be lit by the alcohol lamp burning for the first 20 s in Figure 7b. After removing the alcohol lamp, the shape and volume of the MW had no apparent change. These results indicated that the $MnFe_2O_4$/wood composite was more suitable than the untreated wood and might be applied in building and special decoration materials. This enhanced fire resistance could be ascribed to the special construction of the sample by which the dense $MnFe_2O_4$ layer formed over the cell wall on the wood surface prevented oxidation and heat transfer from proceeding into the inner portion of the wood cell walls, which could be observed from the scanning electron microscope.

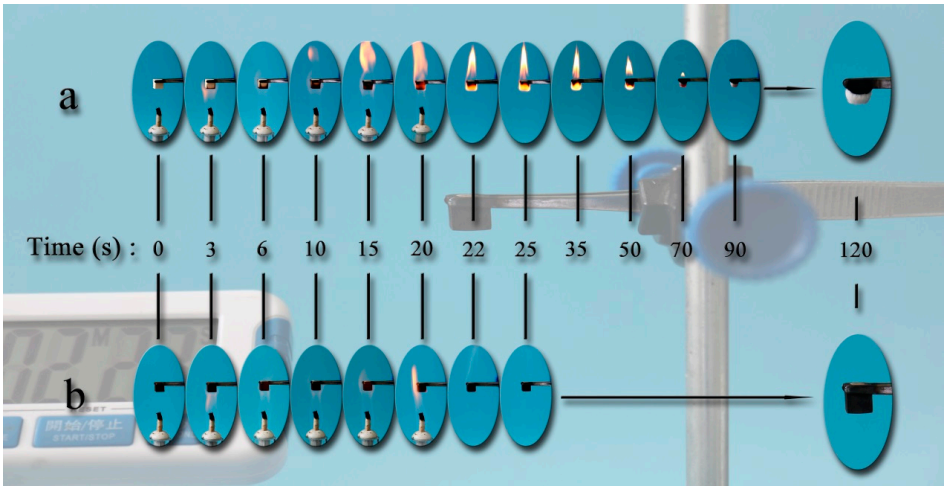

Figure 7. Fire-resistant properties of (**a**) the UW and (**b**) the MW.

To investigate the electromagnetic absorption property of the UW and the MW, the reflection loss (RL) values were calculated by the transmission line theory [41].

$$Z_{in} = Z_0\sqrt{\mu_r/\varepsilon_r}\tanh\left[j\left(\frac{2\pi fd}{c}\right)\sqrt{\mu_r\varepsilon_r}\right] \quad (4)$$

$$\mathrm{RL(dB)} = 20\log\left|\frac{Z_{in}-Z_0}{Z_{in}+Z_0}\right| \quad (5)$$

where Z_{in} is the input impedance of the samples, Z_0 is the impedance of air, μ_r is the complex permeability,ε_r is the complex permittivity, d is the thickness of the samples, f is the frequency of microwaves and c is the velocity of light. Figure 8 shows RL curves of the UW and MW by three-dimensional and color-filling patterns in the frequency range of 2–18 GHz. In Figure 8a, the minimum RL values of the UW reached −3.0 dB at 16.64 GHz, and the RL values of the UW were close to zero at another frequency, which indicated that the main loss mechanism of the UW was only the resonance of the wood at a certain frequency at 16.64 GHz. By contrast, the MW reached −9.3 dB at 16.48 GHz with a thickness of 3 mm in Figure 8b. Moreover, it could be observed that both the minimum reflection loss value and the absorption bandwidth of the $MnFe_2O_4$/wood composite had improved greatly compared with the untreated wood, indicating that the electromagnetic absorption property of the $MnFe_2O_4$/wood composite had been enhanced through the growth of the $MnFe_2O_4$ on the wood. Thus, it might provide a potential application in the field of indoor electromagnetic wave absorbers.

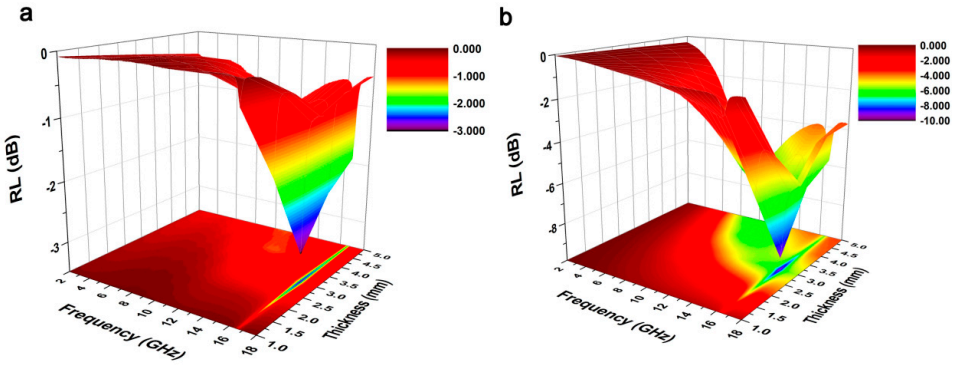

Figure 8. Frequency dependence of the reflection loss (RL) for (**a**) the UW and (**b**) the MW by three-dimensional and color-filling patterns in the frequency range of 2–18 GHz.

4. Conclusions

In summary, we had successfully synthesized the $MnFe_2O_4$/wood composite via a low-temperature hydrothermal method. The nanooctahedra $MnFe_2O_4$ had been tightly located on the wood surface through the hydrogen bonding interactions. The $MnFe_2O_4$/wood composite expressed superior performance of soft magnetism, fire resistance and electromagnetic wave absorption, which could be applied to some fields for special decoration and indoor electromagnetic wave absorption.

Acknowledgments: This research was supported by the Zhejiang Provincial Natural Science Foundation of China under Grant No. LZ15C160002, the Scientific Research Foundation of Zhejiang Agriculture & Forestry University (Grant No. 2014FR077), the Special Fund for Forest Scientific Research in the Public Welfare (Grant No. 201504501) and the Fund for Innovative Research Team of Forestry Engineering Discipline (101-206001000713).

Author Contributions: Qingfeng Sun conceived of the project and revised the whole manuscript. Hanwei Wang, Qiufang Yao and Zhongqing Ma designed the experiments and wrote the paper. Chao Wang, Bitao Fan, and Yipeng Chen prepared Figures 1–8. Chunde Jin provided the project support and revised the partial manuscript. All authors reviewed the manuscript.

Conflicts of Interest: The authors declare that they have no conflict of interest.

References

1. Devi, R.; Maji, T. Interfacial effect of surface modified TiO_2 and SiO_2 nanoparticles reinforcement in the properties of wood polymer clay nanocomposites. *J. Taiwan Inst. Chem. E* **2013**, *44*, 505–514. [CrossRef]
2. Sun, Q.; Lu, Y.; Liu, Y. Growth of hydrophobic TiO_2 on wood surface using a hydrothermal method. *J. Mater. Sci.* **2011**, *46*, 7706–7712. [CrossRef]
3. Devi, R.; Gogoi, K.; Konwar, B.; Maji, T. Synergistic effect of nanoTiO_2 and nanoclay on mechanical, flame retardancy, UV stability, and antibacterial properties of wood polymer composites. *Polym. Bull.* **2013**, *70*, 1397–1413. [CrossRef]
4. Habisreutinger, S.; Schmidt-Mende, L.; Stolarczyk, J. Photocatalytic reduction of CO_2 on TiO_2 and other semiconductors. *Angew. Chem. Int. Ed.* **2013**, *52*, 7372–7408. [CrossRef] [PubMed]
5. Iwamoto, K.; Kamimuta, Y.; Ogawa, A.; Watanabe, Y.; Migita, S.; Mizubayashi, W.; Morita, Y.; Takahashi, M.; Ota, H.; Nabatame, T. Experimental evidence for the flatband voltage shift of high–*k* metal-oxide-semiconductor devices due to the dipole formation at the high–*k*/SiO_2 interface. *Appl. Phys. Lett.* **2008**, *92*, 132907. [CrossRef]
6. Han, C.; Yang, M.; Weng, B.; Xu, Y. Improving the photocatalytic activity and anti-photocorrosion of semiconductor ZnO by coupling with versatile carbon. *Phys. Chem. Chem. Phys.* **2014**, *16*, 16891–16903. [CrossRef] [PubMed]
7. Tanaka, A.; Hashimoto, K.; Kominami, H. Preparation of Au/CeO_2 exhibiting strong surface plasmon resonance effective for selective or chemoselective oxidation of alcohols to aldehydes or ketones in aqueous suspensions under irradiation by green light. *J. Am. Chem. Soc.* **2012**, *134*, 14526–14533. [CrossRef] [PubMed]
8. Gupta, S.; Molian, P. Design of laser micromachined single crystal 6H–SiC diaphragms for high-temperature micro-electro-mechanical-system pressure sensors. *Mater. Des.* **2011**, *32*, 127–132. [CrossRef]
9. Luis, D.L.S.V.; Angel Bustamante, D.; Llandro, J.; Suzuki, S.; Mitrelias, T.; Bellido Quispe, R. Attaching thiolated superconductor grains on gold surfaces for nanoelectronics applications. *Jpn. J. Appl. Phys.* **2010**, *49*, 093102.
10. Pecholt, B.; Molian, P. Nanoindentation of laser micromachined 3C-SiC thin film micro-cantilevers. *Mater. Des.* **2011**, *32*, 3414–3420. [CrossRef]
11. Luis, D.L.S.V.; Angel Bustamante, D.; Quispe, R.B.; Santibañez, W.F.; Aguiar, J.A.; Barnes, C.H.W.; Majima, Y. The Irreversibility Line and Curie-Weiss Temperature of the Superconductor $LaCaBaCu_{3-x}$ $(BO_3)_x$ with x = 0.2 and 0.3. *Phys. Proced.* **2012**, *36*, 354–359.
12. Luis, D.L.D.V.; Angel Bustamante, D.; Gonzalez, J.C.; Juan Feijoo, L.; Ana Osorio, A.; Mitrelias, T. Magnetic properties of the superconductor $LaCaBaCu_3o_7$. *Open Supercond. J.* **2010**, *2*, 19–27.
13. Spinelli, P.; Polman, A. Prospects of near-field plasmonic absorption enhancement in semiconductor materials using embedded Ag nanoparticles. *Opt. Express* **2012**, *20*, A641–A654. [CrossRef] [PubMed]

14. Chen, X.; Liu, J.; Zhang, Z.; Pan, F. Effect of heat treatment on electromagnetic shielding effectiveness of ZK60 magnesium alloy. *Mater. Des.* **2012**, *42*, 327–333. [CrossRef]
15. Tshabalala, M.; Kingshott, P.; VanLandingham, M.; Plackett, D. Surface chemistry and moisture sorption properties of wood coated with multifunctional alkoxysilanes by sol-gel process. *J. Appl. Polym. Sci.* **2003**, *88*, 2828–2841. [CrossRef]
16. Hao, J.; Xu, Z.; Chu, R.; Zhang, Y.; Chen, Q.; Fu, P.; Li, W.; Li, G.; Yin, Q. Characterization of $(K_{0.5}Na_{0.5})$ NbO_3 powders and ceramics prepared by a novel hybrid method of sol–gel and ultrasonic atomization. *Mater. Des.* **2010**, *31*, 3146–3150. [CrossRef]
17. Wang, H.; Zuo, R.; Ji, X.; Xu, Z. Effects of ball milling on microstructure and electrical properties of sol–gel derived $(Bi_{0.5}Na_{0.5})_{0.94}Ba_{0.06}TiO_3$ piezoelectric ceramics. *Mater. Des.* **2010**, *31*, 4403–4407. [CrossRef]
18. Fischer, A.; Pettigrew, K.; Rolison, D.; Stroud, R.; Long, J. Incorporation of homogeneous, nanoscale MnO_2 within ultraporous carbon structures via self-limiting electroless deposition: implications for electrochemical capacitors. *Nano Lett.* **2007**, *7*, 281–286. [CrossRef] [PubMed]
19. Tjeerdsma, B.; Militz, H. Chemical changes in hydrothermal treated wood: FTIR analysis of combined hydrothermal and dry heat-treated wood. *Holz. Roh. Werkst.* **2005**, *63*, 102–111. [CrossRef]
20. Peng, Z.; Sun, Y.; Peng, L. Hydrothermal synthesis of ZrW_2O_8 nanorods and its application in ZrW_2O_8/Cu composites with controllable thermal expansion coefficients. *Mater. Des.* **2014**, *54*, 989–994. [CrossRef]
21. Liu, X.; Zhang, Y.; Xia, X.; Shi, S.; Lu, Y.; Wang, X.; Gu, C.; Tu, J. Self-assembled porous $NiCo_2O_4$ hetero-structure array for electrochemical capacitor. *J. Power Sources* **2013**, *239*, 157–163. [CrossRef]
22. Ezeigwe, E.; Khiew, P.; Siong, C.; Tan, M. Solvothermal synthesis of $NiCo_2O_4$, nanocomposites on liquid-phase exfoliated graphene as an electrode material for electrochemical capacitors. *J. Alloys Compd.* **2016**, *693*, 1133–1142. [CrossRef]
23. Hu, X.; Yu, J.; Gong, J.; Li, Q.; Li, G. α-Fe_2O_3 Nanorings Prepared by a Microwave–Assisted Hydrothermal Process and Their Sensing Properties. *Adv. Mater.* **2007**, *19*, 2324–2329. [CrossRef]
24. Pant, H.; Pant, B.; Sharma, R.; Amarjargal, A.; Kim, H.; Park, C.; Tijing, L.; Kim, C. Antibacterial and photocatalytic properties of Ag/TiO_2/ZnO nano-flowers prepared by facile one-pot hydrothermal process. *Ceram. Int.* **2013**, *39*, 1503–1510. [CrossRef]
25. Kotutha, I.; Swatsitang, E.; Meewassana, W.; Maensiri, S. One-pot hydrothermal synthesis, characterization, and electrochemical properties of rGO/$MnFe_2O_4$ nanocomposites. *Jpn. J. Appl. Phys.* **2015**, *54*, 06FH10. [CrossRef]
26. Phumying, S.; Labuayai, S.; Swatsitang, E.; Amornkitbamrung, V.; Maensiri, S. Nanocrystalline spinel ferrite (MFe_2O_4, M = Ni, Co, Mn, Mg, Zn) powders prepared by a simple aloe vera plant-extracted solution hydrothermal route. *Mater. Res. Bull.* **2013**, *48*, 2060–2065. [CrossRef]
27. Tian, L.; Zhuang, Q.; Li, J.; Wu, C.; Shi, Y.; Sun, S. The production of self-assembled Fe_2O_3–graphene hybrid materials by a hydrothermal process for improved Li-cycling. *Electrochim. Acta* **2012**, *65*, 153–158. [CrossRef]
28. Yao, Q.; Wang, C.; Fan, B.; Wang, H.; Sun, Q.; Jin, C.; Zhang, H. One-step solvothermal deposition of ZnO nanorod arrays on a wood surface for robust superamphiphobic performance and superior ultraviolet resistance. *Sci. Rep.* **2016**, *6*, 35505. [CrossRef] [PubMed]
29. Hosseini, S.; Mohseni, S.; Asadnia, A.; Kerdari, H. Synthesis and microwave absorbing properties of polyaniline/$MnFe_2O_4$ nanocomposite. *J. Alloys Compd.* **2011**, *509*, 4682–4687. [CrossRef]
30. Hong, D.; Yamada, Y.; Nagatomi, T.; Takai, Y.; Fukuzumi, S. Catalysis of nickel ferrite for photocatalytic water oxidation using $[Ru(bpy)_3]^{2+}$ and $S_2O_8^{2-}$. *J. Am. Chem. Soc.* **2012**, *134*, 19572–19575. [CrossRef] [PubMed]
31. Guivar, J.A.R.; Bustamante, A.; Flores, J.; Santillan, M.M.; Osorio, A.M.; Martínez, A.I.; Valladares, L.D.L.S.; Barnes, C.H.W. Mössbauer study of intermediate superparamagnetic relaxation of maghemite (γ-Fe_2O_3) nanoparticles. *Hyperfine Interact.* **2014**, *224*, 89–97. [CrossRef]
32. León, F.L.; Coaquira, J.A.; Martínez, M.A.; Goya, G.F.; Mantilla, J.; Sousa, M.H.; Valladares, L.L.; Barnes, C.H.; Morais, P.C. Structural and magnetic properties of core-shell Au/Fe_3O_4 nanoparticles. *Sci. Rep.* **2017**, *7*, 41732. [CrossRef] [PubMed]
33. Guivar, J.A.R.; Martínez, A.I.; Anaya, A.O.; Valladares, L.D.L.S.; Félix, L.L.; Dominguez, A.B. Structural and Magnetic Properties of Monophasic Maghemite (γ-Fe_2O_3) Nanocrystalline Powder. *Adv. Nanopart.* **2014**, *3*, 114. [CrossRef]

34. Gao, J.; Dai, S.; Li, T. Electronic states of epitaxial thin films of $La_{0.9}Sn_{0.1}MnO_3$ and $La_{0.9}Ca_{0.1}MnO_3$. *Phys. Rev. B* **2003**, *67*, 153403. [CrossRef]
35. Goodarz Naseri, M.; Saion, E.B.; Kamali, A. An overview on nanocrystalline $ZnFe_2O_4$, $MnFe_2O_4$, and $CoFe_2O_4$ synthesized by a thermal treatment method. *ISRN Nanotechnol.* **2012**, *2012*, 604241. [CrossRef]
36. Andrade, P.L.; Silva, V.A.J.; Maciel, J.C.; Santillan, M.M.; Moreno, N.O.; Valladares, L.D.L.S.; Bustamante, A.; Pereira, S.M.B.; Silva, M.P.C.; Aguiar, J.A. Preparation and characterization of cobalt ferrite nanoparticles coated with fucan and oleic acid. *Hyperfine Interact.* **2014**, *224*, 217–225. [CrossRef]
37. Luis, D.L.S.V.; Llandro, J.; Lee, D.; Mitrelias, T.; Palfreyman, J.J.; Hayward, T.J.; Cooper, J.; Bland, J.A.C.; Barnes, C.H.W.; Juan, L.A.C. Magnetic measurements of suspended functionalised ferromagnetic beads under DC applied fields. *J. Magn. Magn. Mater.* **2009**, *321*, 2129–2134.
38. León-Félix, L.; Chaker, J.; Parise, M.; Coaquira, J.A.H.; Valladares, L.D.L.S.; Bustamante, A.; Garg, V.K.; Oliveira, A.C.; Morais, P.C. Synthesis and characterization of uncoated and gold-coated magnetite nanoparticles. *Hyperfine Interact.* **2014**, *224*, 179–188. [CrossRef]
39. Lee, D.; Seo, J.; Valladares, L.D.L.S.; Quispe, O.A.; Barnes, C.H.W. Magnetic and structural properties of yellow europium oxide compound and $Eu(OH)_3$. *J. Solid State Chem.* **2015**, *228*, 141–145. [CrossRef]
40. Llamazares, J.L.S.; Quintananedelcos, A.; Ríosjara, D.; Sánchezvaldes, C.F.; Garcíafernández, T.; García, C. The effect of low temperature thermal annealing on the magnetic properties of Heusler Ni-Mn-Sn melt-spun ribbons. *J. Magn. Magn. Mater.* **2016**, *401*, 38–43. [CrossRef]
41. Caloz, C.; Itoh, T. Application of the transmission line theory of left-handed (LH) materials to the realization of a microstrip "LH line". In Proceedings of the Antennas and Propagation Society International Symposium, San Antonio, TX, USA, 16–21 June 2002; pp. 412–415.